Published in final edited form as:
Langmuir. 2013 July 23; 29(29): 9231–9239. doi:10.1021/la401598e.

CuS_2-Passivated Au-Core, Au_3Cu-Shell Nanoparticles Analyzed by Atomistic-Resolution C_s-Corrected STEM

Subarna Khanal[†], **Gilberto Casillas**[†], **Nabraj Bhattarai**[†], **J. Jesús Velázquez-Salazar**[†], **Ulises Santiago**[†], **Arturo Ponce**[†], **Sergio Mejía-Rosales**[‡], and **Miguel José-Yacamán**[†]

[†]Department of Physics and Astronomy, University of Texas at San Antonio, One UTSA Circle, San Antonio, TX, 78249

[‡]Center for Innovation, Research and Development in Engineering and Technology, and CICFIM-Facultad de Ciencias Físico-Matemáticas, Universidad Autonoma de Nuevo Leon, San Nicolás de los Garza, NL 66450, Mexico

Abstract

Au-core, Au_3Cu-alloyed shell nanoparticles passivated with CuS_2 were fabricated by the polyol method, and characterized by Cs-corrected scanning transmission electron microscopy. The analysis of the high-resolution micrographs reveals that these nanoparticles have decahedral structure with shell periodicity, and that each of the particles is composed by Au core and Au_3Cu alloyed shell surrounded by CuS_2 surface layer. X-ray diffraction measurements and results from numerical simulations confirm these findings. From the atomic resolution micrographs we identified edge dislocations at the twin boundaries of the particles, as well as evidence of the diffusion of Cu atoms into the Au region, and the reordering of the lattice on the surface, close to the vertices of the particle. These defects will impact the atomic and electronic structures thereby changing the physical and chemical properties of the nanoparticles. On the other hand we show for the first time the formation of an ordered superlattice of Au_3Cu and a self-capping layer made using one of the alloy metals. This has significant consequences on the physical mechanism that form multi component nanoparticles.

Keywords

Bimetallic nanoparticles; Core-Shell; Gold; Copper; Au_3Cu; Superlattice; STEM; Molecular dynamics

1. INTRODUCTION

The synthesis of bimetallic (BM) nanoparticles, such as core-shell, heterostructures, or intermetallic and alloyed structures, is an activity that has deserved considerable efforts and attracted tremendous attention from chemists and material scientists alike. Significant work has been done in recent years to control the morphology of these nanostructures, as their physical and chemical properties can be tailored by fine-tuning their chemical composition, structural shape, and size.[1-6] BM nanoparticles are known to exhibit the ability to enhance reactivity, selectivity and stability, depending upon the variation of structure and composition.[7-10] Several synthesis methods for the synthesis of bimetallic particles, both chemical- and physical-based, are well established. The modified polyol method has been extensively used for the synthesis of Au and Au-Cu core-shell nanoparticles. In the latter case, in a first stage Au seeds are synthesized, followed by the reduction of the second metal

Correspondence to: Miguel José-Yacamán.

that will form the shell. The resultant morphology will depend on several factors, including seed size and shape, conditions of reduction of the shell metal, lattice mismatch between the two metals, and volume ratio between seed solution and salt of the shell metal solution.

Cu-based bimetallic nanoparticles are often studied because of their unusual physical and chemical properties compared to those of the monometallic particles. Potential uses of these particles include various catalytic reactions,[8, 11-15] optoelectronics,[16] photothermal therapy,[17] sensing,[18] multimodal imaging and biomedicine,[17, 19, 20] photovoltaic applications,[21-24] and others. However, there are not previous reports that include a detailed structural analysis of these particles. Many experimental works have focused on the controlled synthesis of the core-shell structure nanoparticles to deliberately tailor their properties; most of these articles report the synthesis of nanoparticles constituted by Au-Cu,[13, 25-31] Au-Cu_2O,[32-35] and Au-Cu_2S,[7, 8, 10, 11, 36], either with a core–shell distribution, random alloy, or heterostructures. The more common gold and copper superlattices have stoichiometries AuCu and $AuCu_3$, while the superlattice Au_3Cu with a face centered cubic packing is rarely observed.

In this work, we present a comprehensive experimental investigation on Au-core, Au_3Cu-alloyed shell nanoparticles passivated with CuS_2 surface layer, of sizes under 50 nm. To the best of our knowledge, this is the first report with this kind of composition and structure. The nanoparticles were analyzed by transmission electron microscopy (TEM), and by aberration-corrected scanning transmission electron microscopy (Cs-STEM), in combination with high angle annular dark field (HAADF), bright field (BF) and energy dispersive X-ray spectroscopy (EDS) detectors. The HAADF intensity profiles reveal that there is diffusion of the Cu atoms into the Au lattice site, and that edge dislocations appear in the twin boundaries of the decahedral structure, as an effect of the inhomogeneous elastic strain.[37]

2. EXPERIMENTAL SECTION

2.1. Chemicals and Materials

Chemicals from Aldrich and Sigma Aldrich were used in the experimental processes. Gold (III) Chloride Trihydrate ($HAuCl_4.xH_2O$, > 99.9+ %), Copper (II) Sulfate Anhydrous ($CuSO_4$, >90.0%), Poly (vinylpyrrolidone) (PVP, Mw = 55K), Ethylene glycol (EG, >99.5%) was used as both the solvent and reducing agent. Solvents as ethanol and acetone were used for cleaning purposes. Only chemicals of analytical grade were used, without any further purification process.

2.1. Synthesis of Au Seeds

As a first stage, Au nanoparticles were synthesized by the polyol method: A volume of 25 mL of ethylene glycol (EG) and 2 gm of PVP (55K) was mixed and vigorously stirred in a round-bottom flask for 10 min and refluxed at 200 °C using a hot oil bath. 0.025 M of 2 mL $HAuCl_4.xH_2O$ were added to the solution using a syringe pump, and the resulting mixture was stirred vigorously and refluxed for 5 min. At this point the solution turned purple-red color, evidencing the formation of Au nanoparticles. Ulterior TEM analysis showed that the range of sizes of these seeds was of 30 to 35 nm, with approximately 80% of the population having decahedral shapes (see Figure 1).

2.2. Synthesis of the Core-Shell Particles

The Au nanoparticles were used as seeds for the growth of bimetallic nanoparticles. 14 mL of EG solution and 249 mM of PVP (55K) were mixed in a three-neck round-bottom flask and refluxed for 10 min. at a constant temperature of 200 °C under Argon ambient. The solution was mixed with 3 mL of the recently prepared solution containing the Au seeds,

and the mixture was kept under magnetic stirring for 10 min. Afterwards, a solution of 50 mM of CuSO4 and 3 mL of EG was injected drop by drop using a syringe pump, and the resulting mixture was stirred vigorously and refluxed for 1h at 200 °C in Argon ambient. After 1h the mixture solution turned brown-blue color, evidencing the formation of the bimetallic nanoparticles. The solution was washed by adding 1 mL of the solution to 9 mL of ethanol and was centrifuged at 6000 rpm for 10 minutes. This process of centrifuging was repeated three times, adding acetone prior to the last centrifuging cycle. The precipitate was collected and re-dispersed with ethanol. The resulting particles were drop-casted onto 3 mm copper grids for their subsequent characterization.

2.3. Characterization

A JEOL 1230 microscope operated at 120 kV was employed to obtain the TEM micrographs used to study the morphology of the particles. The STEM images were obtained with a Cs-corrected JEOL JEM-ARM 200F operated at 200 kV, using a HAADF detector, with a convergence angle of 26 mrad and collection semi-angles from 50 to 180 mrad, in order to eliminate contributions from unscattered and low-angle scattered electron beams. The probe size was about 0.09 nm with a probe current of 22 pA. Additionally, BF STEM images were recorded using a detector working at a maximum collection semi-angle of 11 mrad. EDS spectra were obtained using a probe size of 0.13 nm with the probe current 86 pA. Absorption spectra in the 400-700 nm range were measured by using a UV-Visible spectrophotometer (Cary, Model 14R). The samples were prepared for X-ray diffraction (XRD) measurements by drying the nanoparticles solutions and disperse them on a glass substrate. The XRD analysis was made using a RIGAKU Ultima IV X-ray diffractometer with Cu-Kα (λ = 1.54056 Å) working at 40 kV and 30 mA in the parallel beam configuration.

3. RESULTS AND DISCUSSION

The polyol method produced gold nanoparticles of several morphologies: a mixture of decahedral, icosahedral, triangular plates, and rods. Figure 1a is a composed image made of low magnification TEM bright-field representative micrographs, showing these morphologies. The fraction of decahedral, icosahedral, triangular plates, and rods nanoparticles were 76, 16, 7, and 1 % respectively, as shown in the histogram Figure 1b. The average size of the nanoparticles was ~35 nm. The decahedral, icosahedral, and rod-like particles are multiple-twinned, while the triangular plates are single-twinned. With the exception of the scarce nanorods, all these nanoparticles have {111} planes as major facets. Since the majority of the seed particles were decahedral, the characterization study was focused on the particles with this geometry. Figure 2a is composed by four TEM micrographs containing the images of several core-shell nanostructures synthesized using the Au nanoparticles as seeds. The final morphology of the particles depended on the shape of the seed: particles that grew out of decahedral seeds were also decahedral, although the orientation of a decahedral particle did not coincide with the orientation of its decahedral seed; because of this, the final nanoparticles have a star-like appearance, as can be noted in the particles on Figure 2a. The elemental distribution in the nanostructure is investigated using EDS line scan and is presented in Figure S1 in supporting information (SI). The line scan in the interface region revealed the presence of Au and Cu (SI Figure S1(a) and (b), while the line scan along the core-shell region with surface layer showed the presence of Au, Cu and S signal (SI Figure S1(c) and (d)). We added the EDS mapping corresponding to surface layer, which shows only the presence of Cu and S signals (SI Figure S2). 100μL of the as-prepared colloid solutions of both gold and core-shell particles were separately mixed with 3mL of ethanol, to be used for obtaining their UV-vis absorption spectra. The results are shown in Figure 2b. Neither sample exhibited apparent near-infrared (NIR) absorbance. The Au and core-shell particles have surface plasmon resonance (SPR) peaks centered at

around 544 nm and 574 nm respectively. The significant red shift of the signal of the BM nanoparticles confirms a change in the composition and crystal structure with respect to the gold particles. This red shift of on the SPR absorption was observed to depend on the copper concentration and it appears to be a dielectric effect, because of the presence of copper sulfide materials of high refractive index attached to the Au cores.

Since in STEM, the HAADF intensity signal depends not just on the amount of material but also on the elements present in the atomic column parallel to the electron beam,[38] this technique is a very suitable choice for the analysis of the composition of the nanoparticles. An aberration-corrected HAADF image of a decahedral core-shell nanoparticle is shown in Figure 3a, and the inset shows a model of the core-shell decahedral structure. Three regions are clearly distinguishable from each other: the Au core, a highly ordered alloyed shell in interface with the core, and a capping of what appears to be CuS_2 lattices at the surface. These CuS_2 surface layers, labeled as T_1 through T_5 in Figure 3a, may have a thickness as large as 5 ± 0.7 nm (see SI Figure S3). Figure 3b shows close-ups of the five {100} surfaces of the decahedral nanoparticles revealing that each one of them present a diffuse interface boundary that forms the shell region composed by Au and Cu atoms. A single layer of Cu diffuses into the Au {111} surface (marked by red arrows) in the T_1, T_2 and T_4 regions. At the T_3 region appears a defect in the lattice structure in addition to the diffusion of the Cu atoms into the Au lattices, likely to be an effect of the lattice mismatch between Au and Cu (11.4%). Interestingly, diffusion of the Cu on Au surface is quite different in the T_5 region, where we can observe three layers of Cu interpenetrated into the Au surface (marked by red arrows), while on the left side of the same Au{111} surface only one layer of the Cu is interpenetrated into the Au surface. This also happens because of the lattice mismatch between the Au and Cu. As a consequence of the interpenetration, the crystal structure of the interface regions get formed by ordered single crystals of Au_3Cu face centered cubic (fcc) alloy structure.

Figure 4a shows a HAADF-STEM micrograph of the copper sulfide passivated surface region T_5 shown in Figure 3b. Here the difference in intensity in the atomic columns of the core, compared against the diffused shell regions, becomes evident. The insets show the fast Fourier transform (FFT) patterns of Au core (at the right top corner of Figure 4a) and CuS_2 surface layer (right bottom corner of Figure 4a) regions. The lattice spacing measured at the core region is 0.236 nm, which agrees well with the inter-{111} lattice spacing of Au crystals. Likewise, the low intensity region (CuS_2 surface layer) exhibits a lattice spacing of 0.286 nm, which is consistent with the nominal spacing of {200} planes of cubic CuS_2 0.288 nm.[39] A close-up of the diffuse interphase boundary is shown in Figure 4b, revealing that the composition of the individual columns can be corroborated by the changes in the intensity signal. The interphase boundary diffusion of Cu on the Au surfaces can be directly observed in the aberration corrected STEM micrograph. Moreover, this structure exhibits not only the diffuse interphase but also the epitaxial growth of surface capping CuS_2 lattices, albeit a large lattice mismatch (11.4%) between Au (0.4079 nm) and Cu (0.3615 nm). There is previous evidence of this kind of growth: Tsuji *et al.*[31] demonstrated that the shells can be overgrown epitaxially on the cores even when there is a lattice mismatch of more than 10% in core-shell BM nanoparticle. In our case, the large lattice mismatch between Au and Cu creates strong static lattice distortions, allowing a well-known mechanical relaxation and stress-induced diffusion.[40, 41] Another possible reason for strain is the lattice contraction of surface atoms.[42] Measurements at the diffused interface region shown in Figure 4b gave lattice spacing of 0.225 nm (Au-Cu), 0.380 nm (Au-Au) and 0.281 nm (Cu-Cu), which can be related to the inter lattice spacing of {111}, {100}, and {110} planes in the face centered cubic (fcc) Au_3Cu alloy structure, respectively (see Figure S4 of SI), since the nominal values of this lattice spacing in Au_3Cu are 0.229 nm (Au-Cu, {111} planes), 0.398 nm (Au-Au, {100} planes) and 0.281 nm (Cu-Cu, {110} planes) respectively (JCPDS card no.

01-071-5023). XRD patterns measured in both the Au nanoparticles and the core-shell nanoparticles (SI Figure S5) correspond to a face centered cubic (fcc) crystal structure revealing the presence of (111), (200), (220), (311) and (222) reflections with peaks at 2θ values of 38.24°, 44.32°, 64.81°, 77.76° and 81.98° respectively. These XRD reflection peaks match the standard pattern for Au and Au_3Cu. Thus, these results also support the notion that the nanoparticles have a composition of Au-core, Au_3Cu alloy-shell, with the surface passivated by a CuS_2 lattice that stabilizes the crystal structure.

Figure 5a shows a magnified atomic resolution HAADF-STEM image of the interface region, where it is possible to distinguish the intensities due to the presence of Au (bright zone) and from the intensities due to CuS_2 (Light zone) lattices. It is also possible to observe Cu layer interpenetrated into the Au lattice. The atomistic model was constructed to exemplify the structure (Figure 5a) which is shown in Figure 5b where an Au-core, Au_3Cu alloyed shell and CuS_2 surface layer is evident. This CuS_2 surface layer matched with the experimental atomic resolution micrograph (See also SI Figure S6). The atomistic model (Figure 5b) was used to generate the simulated STEM image shown in Figure 5c. These results between simulated structures with those observed experimentally are in very good agreement. The intensity profiles of Figure 5d correspond to the lines labeled as X (Au_3Cu alloyed shell region) and Y (CuS_2 surface layer region); here, it can be noted the dramatic difference in the intensity due to the differences in atomic number. The average distance between Au-Cu peaks is 0.225 nm, and 0.199 nm for Cu-S; these values are consistent with an Au_3Cu alloy {111} plane and a CuS_2 surface layer {200} plane respectively.

The decahedral nanoparticles showed other very interesting features. While Tsuji *et al*. did not observe interpenetration of the Cu on Au surface; we observed variations in intensity at the regions where adjacent tetrahedral subunits interface in a twin boundary, that we interpret as Cu atoms interpenetrated into the Au surfaces. Figure 6a shows an atomic resolution HAADF STEM image of this type of particles, in a [011] zone axis. A perfect decahedral crystal structure is composed of five fcc tetrahedral single crystal structures, joined together on adjacent {111} planes and forming an angle between two (111) planes of 70.58°, leaving a 7.35° solid angle deficiency. In order to fulfill the solid angle deficiency, the incorporation of homogeneous elastic strain,[43] an inhomogeneous strain,[44] or a structural modification [45, 46] is necessary to stabilize the decahedral structure. Nonetheless, the structural defects and dislocations are arising from lattice mismatch,[47] especially in the twin boundaries. The interpenetration of Cu atoms on Au decahedral twin boundaries create the structural defects, the lattice mismatch between Au and Cu (11.4%) give raise to the edge dislocation at the twin boundary (marked by the “T” and the red lines) as shown in Figure 6(b-d). The significant difference of the lattice parameter of Au and Cu generate internal strain on the BM system. In contrast, no edge dislocations were observed at the twin boundaries shown at Figure 6e and 6f. Moreover, the intensity profile analysis of the twin boundary in Figure 6f (marked by a white arrow) shown in Figure 6g reveals the disparity of intensities between Au-rich and Cu-rich atomic columns, where the Cu rich atomic columns have lesser intensity in comparison to the Au rich atomic columns as a consequence of the difference in their respective atomic numbers.

A second feature that can be easily detected in the micrographs of Figure 6 is the apparent mismatch of the lattice in the vicinity of the vertices of the particle. This feature is particularly easy to note in Figure 6e, although it is practically present on the whole border of the particle. In order to try to explain the characteristics of these regions, the particles were modeled through a series of molecular dynamics (MD) runs in the canonical ensemble, using a Sutton-Chen potential to describe the metal-metal interactions.[48] A model particle was prepared following the decahedral geometry of the real particles and their chemical composition: An Au core surrounded by a AuCu shell in a 3:1 proportion. To avoid a

computationally expensive set of MD calculations, the model particle was smaller in size than the real particles, having a size of approximately 10 nm, and 13025 atoms in total. The MD conventional techniques have an inherent restriction on the time length of the dynamical trajectory generated by the simulation, which implies that, when the simulation is made at low temperatures, the sampling of the configurational space is made at a slow pace, because the atoms have to overcome potential energy barriers too high, compared to kT. While techniques based on random sampling are able to deal with this restriction by ignoring the energetic barriers between two configurations, samplings made through MD simulations require either to redefine the interatomic potentials to lower the energetic barriers, or to use higher values of temperature to ease the diffusion of the atoms. Since in this case the interest on the simulation relays not in the specific dynamic trajectory of the particle, but on the generation of configurations that would take a long simulation time to reach at low T, we decided to raise the temperature in an escalated manner from 300K until 800K to promote the atomic diffusion of the atoms at the surface of the particle. The configurations obtained with the MD runs were used as input for the simulation of STEM micrographs, following the multislice method.[49] A typical configuration of the particle is shown in Figure 7a in a representation that allows to perceive easily the details on the surface and borders of the particle. It is not difficult to note that, as a result of the migration of atoms that originally were located at the vertices and borders of the decahedron, an additional atomic layer has been formed close to the border of the particle. Analysis of the whole MD trajectory (7.5 ns in total) shows that these layers are not completely static, but they are constantly reconstructing themselves, via migration of atoms and exchange of atomic positions. The simulated STEM micrograph of the structure shown in Figure 7a is in Figure 7b, and the regions corresponding to the partial layers are marked with white ovals. By the comparison of this simulated STEM image with the real micrographs of Figure 6, we were able to correlate the lattice mismatches in the real particles with the partial layer formed in the surface of the simulated particle by the migration of the atoms originally at the vicinity of the vertices.

4. CONCLUSIONS

We synthesized Au core and Au_3Cu alloyed shell nanoparticles passivated with CuS_2 layers by using modified polyol method. The prevalent geometry in these particles is the decahedral, with a small representation of triangular, icosahedral and rod-like particles. Atomic resolution TEM and Cs-corrected STEM imaging confirm the core-shell distribution of the metals in the particle, and detailed measurements of interplanar distances in combination with XRD analysis allowed us to conclude that the particles are indeed formed by Au seeds surrounded by Au_3Cu superlattice, and surface passivated with CuS_2 layers. At atomistic level, the diffusion of Cu atoms into the Au lattice site and the lattice mismatch between them leads to the formation of alloyed structure. The significant difference of the lattice parameter generates internal strain on the BM system. The formation of edge dislocation in decahedral nanostructure can be explained from the strain release mechanism and different atomic sizes of Au and Cu atoms stabilize the dislocation in the twin boundaries.[50, 51] Some of the material from the vertices of the particles migrate to form partial atomic layers at the vicinity of the borders of the decahedra, as it was found by comparison of STEM micrographs with results from molecular dynamics simulations.

Supplementary Material

Refer to Web version on PubMed Central for supplementary material.

Acknowledgments

This project was supported by grants from the National Center for Research Resources (5 G12RR013646-12) and the National Institute on Minority Health and Health Disparities (G12MD007591), from the National Institutes of Health. and from the NSF for support with grants DMR-1103730, “Alloys at the Nanoscale: The Case of Nanoparticles Second Phase and PREM: NSF PREM Grant # DMR 0934218; Support from the Mexican Council for Science and Technology (CONACYT, Mexico), through project CIAM 148967, is also acknowledged.

References

1. Pearson, WB. The crystal chemistry and physics of metals and alloys. Wiley-Interscience; New York: 1972.
2. Toshima N, Yonezawa T. Bimetallic nanoparticles-novel materials for chemical and physical applications. New J Chem. 1998; 22:1179–1201.
3. Daniel M-C, Astruc D. Gold Nanoparticles: Assembly, Supramolecular Chemistry, Quantum-Size-Related Properties, and Applications toward Biology, Catalysis, and Nanotechnology. Chem Rev. 2003; 104:293–346. [PubMed: 14719978]
4. Ferrando R, Jellinek J, Johnston RL. Nanoalloys: From Theory to Applications of Alloy Clusters and Nanoparticles. Chem Rev. 2008; 108:845–910. [PubMed: 18335972]
5. Wang G, Van Hove MA, Ross PN, Baskes MI. Quantitative prediction of surface segregation in bimetallic Pt–M alloy nanoparticles (M = Ni, Re, Mo). Prog Surf Sci. 2005; 79:28–45.
6. Khanal S, Casillas G, Velazquez-Salazar JJ, Ponce A, Jose-Yacaman M. Atomic Resolution Imaging of Polyhedral PtPd Core–Shell Nanoparticles by Cs-Corrected STEM. J Phys Chem C. 2012; 116:23596–23602.
7. Carbone L, Cozzoli PD. Colloidal heterostructured nanocrystals: Synthesis and growth mechanisms. Nano Today. 2010; 5:449–493.
8. Motl NE, Bondi JF, Schaak RE. Synthesis of Colloidal Au–Cu2S Heterodimers via Chemically Triggered Phase Segregation of AuCu Nanoparticles. Chem Mater. 2012; 24:1552–1554.
9. Shen S, Tang Z, Liu Q, Wang X. Precisely Controlled Growth of Heterostructured Nanocrystals via a Dissolution–Attachment Process. Inorg Chem. 2010; 49:7799–7807. [PubMed: 20681592]
10. Ghosh CR, Paria S. Core/shell nanoparticles: classes, properties, synthesis mechanisms, characterization, and applications. Chem Rev. 2012; 112:2373. [PubMed: 22204603]
11. Ding X, Zou Y, Jiang J. Au-Cu2S heterodimer formation via oxidization of AuCu alloy nanoparticles and in situ formed copper thiolate. J Mater Chem. 2012; 22:23169–23174.
12. Kim Y, Park KY, Jang DM, Song YM, Kim HS, Cho YJ, Myung Y, Park J. Synthesis of Au–Cu2S Core–Shell Nanocrystals and Their Photocatalytic and Electrocatalytic Activity. J Phys Chem C. 2010; 114:22141–22146.
13. Yin J, Shan S, Yang L, Mott D, Malis O, Petkov V, Cai F, Shan Ng M, Luo J, Chen BH, Engelhard M, Zhong C-J. Gold–Copper Nanoparticles: Nanostructural Evolution and Bifunctional Catalytic Sites. Chem Mater. 2012; 24:4662–4674.
14. Liu X, Wang A, Wang X, Mou C-Y, Zhang T. Au-Cu Alloy nanoparticles confined in SBA-15 as a highly efficient catalyst for CO oxidation. Chem Commun. 2008; 0:3187–3189.
15. Bracey CL, Ellis PR, Hutchings GJ. Application of copper-gold alloys in catalysis: current status and future perspectives. Chem Soc Rev. 2009; 38:2231–2243. [PubMed: 19623346]
16. Talapin DV, Lee J-S, Kovalenko MV, Shevchenko EV. Prospects of Colloidal Nanocrystals for Electronic and Optoelectronic Applications. Chem Rev. 2009; 110:389–458. [PubMed: 19958036]
17. Lakshmanan SB, Zou X, Hossu M, Ma L, Yang C, Chen W. Local Field Enhanced Au/CuS Nanocomposites as Efficient Photothermal Transducer Agents for Cancer Treatment. J Biomed Nanotechnol. 2012; 8:883–890. [PubMed: 23029996]
18. Macdonald JE, Bar Sadan M, Houben L, Popov I, Banin U. Hybrid nanoscale inorganic cages. Nat Mater. 2010; 9:810–815. [PubMed: 20852616]
19. Ghosh Chaudhuri R, Paria S. Core/Shell Nanoparticles: Classes, Properties, Synthesis Mechanisms, Characterization, and Applications. Chem Rev. 2011; 112:2373–2433. [PubMed: 22204603]

20. Zhou M, Zhang R, Huang M, Lu W, Song S, Melancon MP, Tian M, Liang D, Li C. A Chelator-Free Multifunctional [64Cu]CuS Nanoparticle Platform for Simultaneous Micro-PET/CT Imaging and Photothermal Ablation Therapy. J Am Chem Soc. 2010; 132:15351–15358. [PubMed: 20942456]
21. Lee H, Yoon SW, Kim EJ, Park J. In-Situ Growth of Copper Sulfide Nanocrystals on Multiwalled Carbon Nanotubes and Their Application as Novel Solar Cell and Amperometric Glucose Sensor Materials. Nano Lett. 2007; 7:778–784. [PubMed: 17324003]
22. Neville, RC. Solar Energy Conversion: The Solar Cell. Elsevier Science; 1995.
23. Page M, Niitsoo O, Itzhaik Y, Cahen D, Hodes G. Copper sulfide as a light absorber in wet-chemical synthesized extremely thin absorber (ETA) solar cells. Energ Environ Sci. 2009; 2:220–223.
24. Wu Y, Wadia C, Ma W, Sadtler B, Alivisatos AP. Synthesis and Photovoltaic Application of Copper(I) Sulfide Nanocrystals. Nano Lett. 2008; 8:2551–2555. [PubMed: 18651779]
25. Sra AK, Schaak RE. Synthesis of atomically ordered AuCu and AuCu3 nanocrystals from bimetallic nanoparticle precursors. J Am Chem Soc. 2004; 126:6667–6672. [PubMed: 15161294]
26. Hennig J, Mari D, Schaller R. Order-disorder phase transition and stress-induced diffusion in Au-Cu. Phys Rev B. 2009; 79:144116.
27. Alvarez-Paneque AF, Rodríguez-González B, Pastoriza-Santos I, Liz-Marzán LM. Shape-Templated Growth of Au@Cu Nanoparticles. J Phys Chem C. 2012; 117:2474.
28. Ascencio JA, Liu HB, Pal U, Medina A, Wang ZL. Transmission electron microscopy and theoretical analysis of AuCu nanoparticles: Atomic distribution and dynamic behavior. Microsc Res Techniq. 2006; 69:522–530.
29. Dilshad N, Ansari MS, Beamson G, Schiffrin DJ. Amines as dual function ligands in the two-phase synthesis of stable AuxCu(1-x) binary nanoalloys. J Mater Chem. 2012; 22:10514–10524.
30. Motl NE, Ewusi-Annan E, Sines IT, Jensen L, Schaak RE. Au–Cu Alloy Nanoparticles with Tunable Compositions and Plasmonic Properties: Experimental Determination of Composition and Correlation with Theory. J Phys Chem C. 2010; 114:19263–19269.
31. Tsuji M, Yamaguchi D, Matsunaga M, Alam MJ. Epitaxial Growth of Au@Cu Core–Shell Nanocrystals Prepared Using the PVP-Assisted Polyol Reduction Method. Cryst Growth Des. 2010; 10:5129–5135.
32. Zhang L, Blom DA, Wang H. Au–Cu2O Core–Shell Nanoparticles: A Hybrid Metal-Semiconductor Heteronanostructure with Geometrically Tunable Optical Properties. Chem Mater. 2011; 23:4587–4598.
33. Zhang L, Jing H, Boisvert G, He JZ, Wang H. Geometry Control and Optical Tunability of Metal–Cuprous Oxide Core–Shell Nanoparticles. ACS Nano. 2012; 6:3514–3527. [PubMed: 22443453]
34. Kuo C-H, Yang Y-C, Gwo S, Huang MH. Facet-Dependent and Au Nanocrystal-Enhanced Electrical and Photocatalytic Properties of Au–Cu2O Core–Shell Heterostructures. J Am Chem Soc. 2010; 133:1052–1057. [PubMed: 21174406]
35. Wang YQ, Nikitin K, McComb DW. Fabrication of Au-Cu2O core-shell nanocube heterostructures. Chem Phys Lett. 2008; 456:202–205.
36. Cozzoli PD, Pellegrino T, Manna L. Synthesis, properties and perspectives of hybrid nanocrystal structures. Chem Soc Rev. 2006; 35:1195–1208. [PubMed: 17057845]
37. Howie A, Marks L. Elastic strains and the energy balance for multiply twinned particles. Philos Mag A. 1984; 49:95–109.
38. Pennycook S. Z-contrast STEM for materials science. Ultramicroscopy. 1989; 30(1-2):58–69.
39. King HE, Prewitt CT. Structure and symmetry of CuS 2 (pyrite structure). Am Mineral. 1979; 64:1265–1271.
40. Frenkel AI, Machavariani VS, Rubshtein A, Rosenberg Y, Voronel A, Stern EA. Local structure of disordered Au-Cu and Au-Ag alloys. Phys Rev B. 2000; 62:9364–9371.
41. Zener C. Stress Induced Preferential Orientation of Pairs of Solute Atoms in Metallic Solid Solution. Phys Rev. 1947; 71:34–38.

42. Huang W, Sun R, Tao J, Menard L, Nuzzo R, Zuo J. Coordination-dependent surface atomic contraction in nanocrystals revealed by coherent diffraction. Nat mater. 2008; 7:308–313. [PubMed: 18327263]
43. Ino S. STABILITY OF MULTIPLY-TWINNED PARTICLES. J Phys Soc Jap. 1969; 27:941.
44. Wit R. Partial disclinations. J Phys C Solid State. 1972; 5:529.
45. Heinemann K, Yacaman M, Yang C, Poppa H. The structure of small, vapor-deposited particles: : I. Experimental study of single crystals and particles with pentagonal profiles. J cryst growth. 1979; 47:177–186.
46. Yacamán MJ, Heinemann K, Yang CY, Poppa H. The structure of small, vapor-deposited particles: II. Experimental study of particles with hexagonal profile. J cryst growth. 1979; 47:187–195.
47. Bhattarai N, Casillas G, Ponce A, Jose-Yacaman M. Strain-release mechanisms in bimetallic core-shell nanoparticles as revealed by Cs-corrected STEM. Surf Sci. 2012; 609:161–166. [PubMed: 23457419]
48. Rafii-Tabar H, Sulton A. Long-range Finnis-Sinclair potentials for fcc metallic alloys. Philos Mag Lett. 1991; 63:217–224.
49. Ishizuka K. A practical approach for STEM image simulation based on the FFT multislice method. Ultramicroscopy. 2002; 90:71–83. [PubMed: 11942640]
50. Ding Y, Sun X, Lin Wang Z, Sun S. Misfit dislocations in multimetallic core-shelled nanoparticles. Appl Phys Lett. 2012; 100:111603–111603-4.
51. Wu J, Li P, Pan Y-T, Warren S, Yin X, Yang H. Surface lattice-engineered bimetallic nanoparticles and their catalytic properties. Chem Soc Rev. 2012; 41:8066–8074. [PubMed: 23104135]

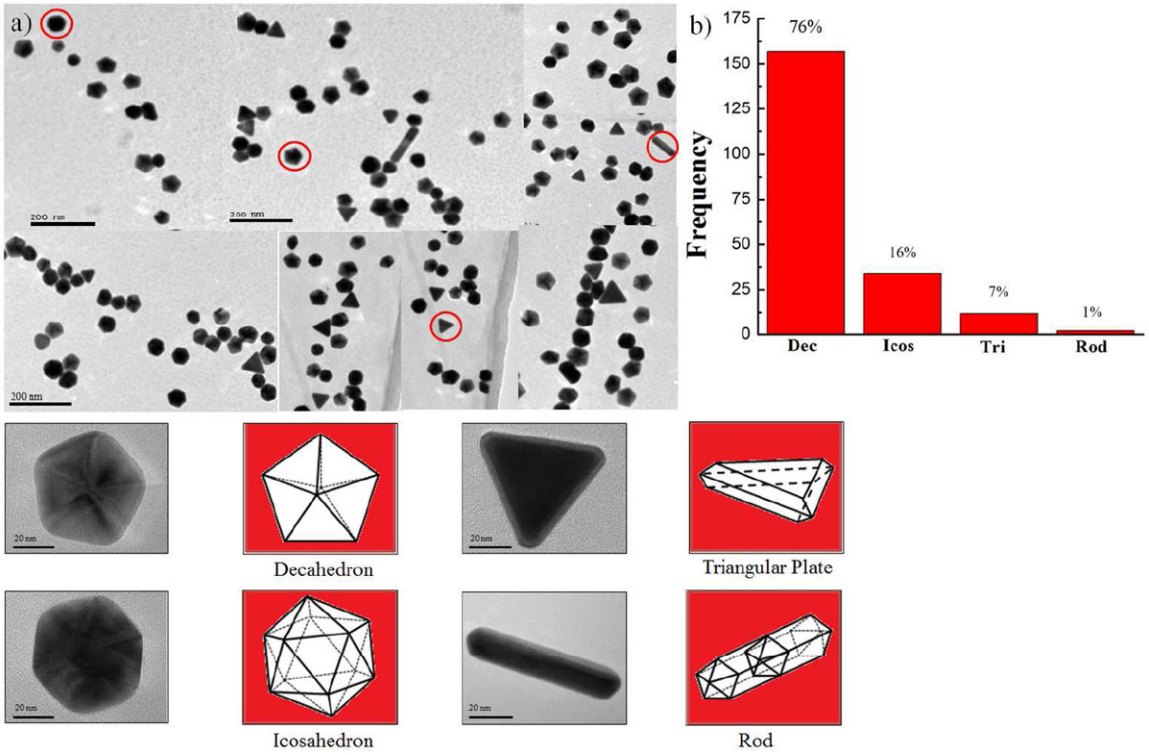

Figure 1.

(a) Low-magnification TEM image of the Au nanoparticles, (b) The histogram for morphology distribution of decahedron, icosahedron, triangular plate, and rod.

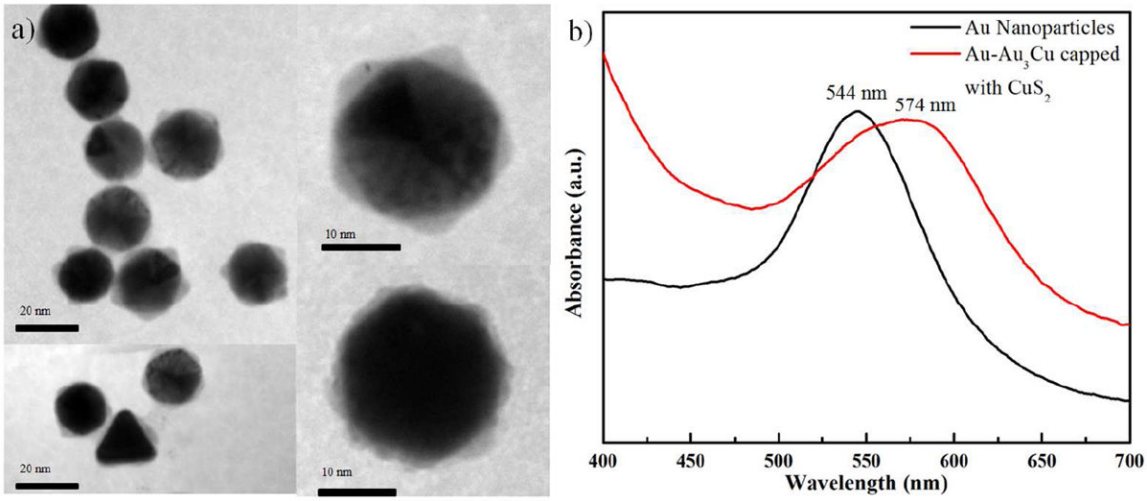

Figure 2.

(a) TEM images of the Au core and Au3Cu alloyed shell nanoparticles passivated with CuS2 surface layers with different morphology, where the growth of Au3Cu follows in (111) surfaces, (b) UV-Vis absorption spectra of bimetallic nanoparticles.

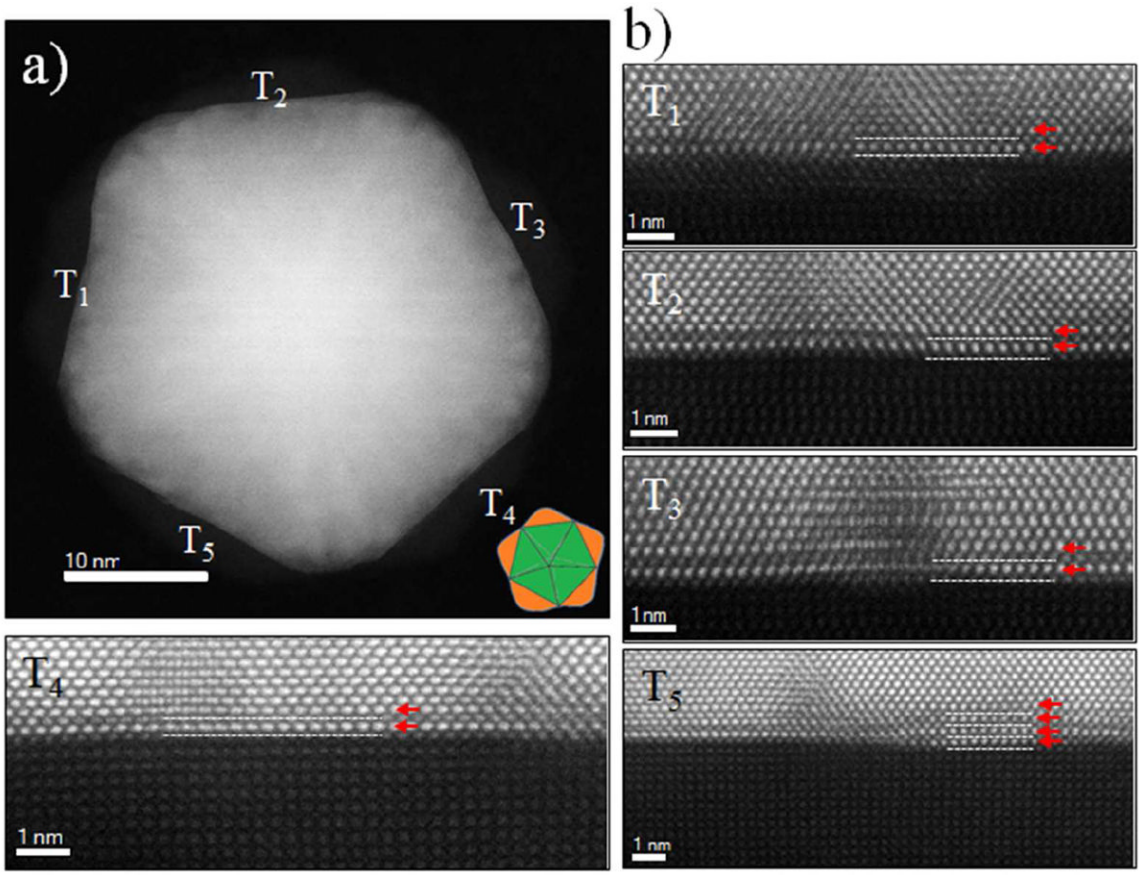

Figure 3.
(a) Atomic-resolution HAADF-STEM image of a decahedral core–shell nanoparticle in a [011] zone axis, (b) Close-ups of the interface regions where the lattice diffusion are readily observed.

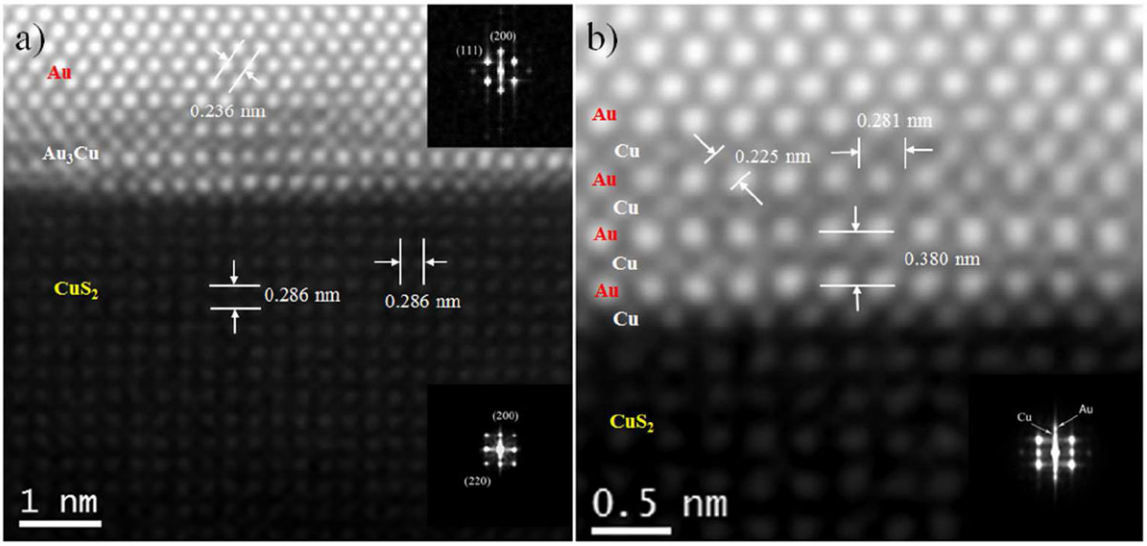

Figure 4.

(a) Atomic-resolution HAADF-STEM image of core–shell nanoparticle different contrast exhibits Au-core, ordered Au3Cu interface region, and CuS2 surface layer, the corresponding inset fast Fourier transform (FFT) patterns exhibits the Au-core and CuS2 surface layer, (b) Close-up of the ordered Au3Cu alloyed shell region where the different contrasts of Au and Cu lattices are readily observable and inset shows the FFT of alloyed shell region.

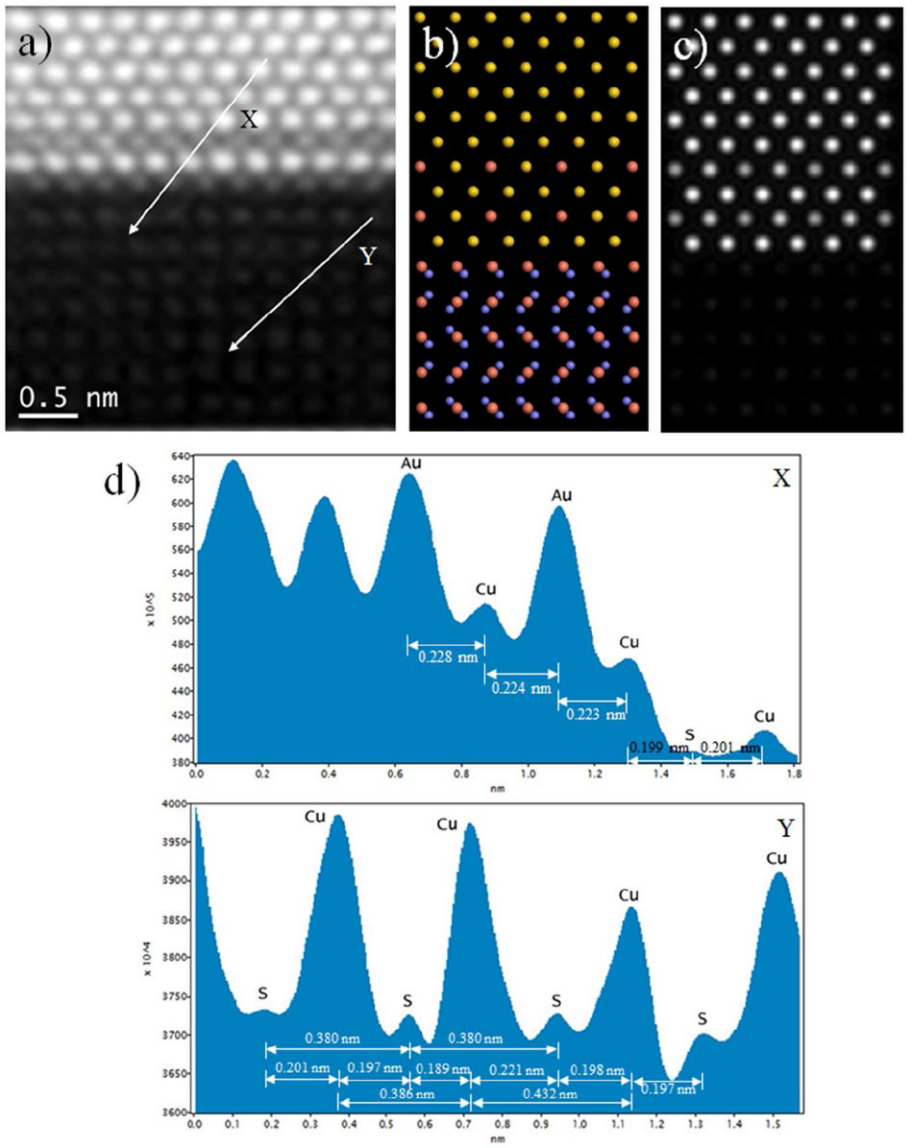

Figure 5.

(a) Atomic-resolution HAADF image of core–shell nanoparticle interface region oriented along [011] direction, (b) The model structures exhibits the Au, diffusion of the Cu atoms into the Au lattice site in shell region (Au3Cu alloy) and CuS2 surface layer, where yellow, pink and light blue spheres represents Au, Cu and S atoms respectively, (c) Simulated STEM micrograph from model (b) and (d) Intensity profiles of shell region (Au3Cu alloy) and CuS2 surface layer shows the disparity of the intensity in the atomic columns can be observed. It should be noted that Au, Cu and S indicated in the intensity line profile represents Au-rich, Cu-rich and S-rich atomic columns.

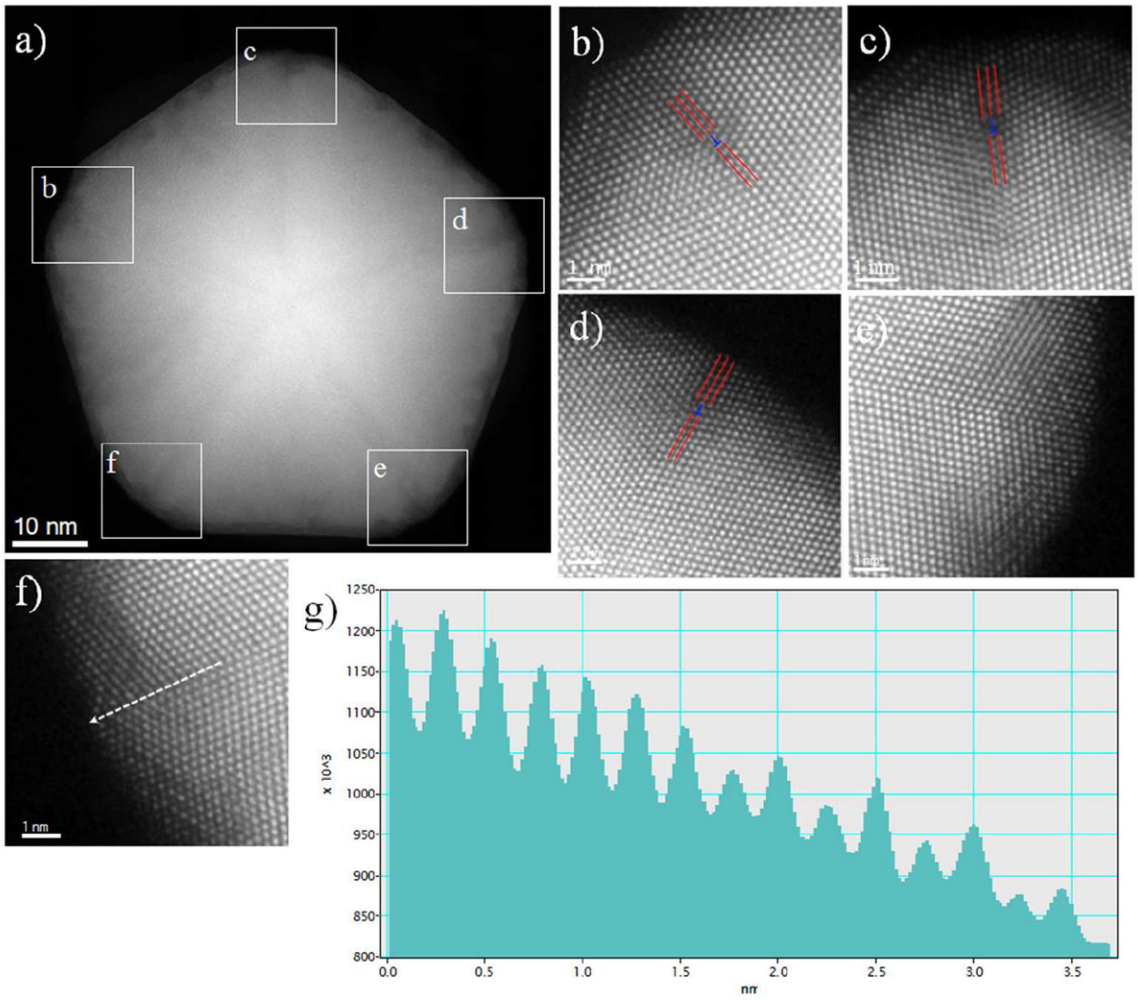

Figure 6.

(a) HAADF image of decahedral core-shell nanoparticles in a [011] zone axis, (b – f) Amplified images of the square area of Figure 6(a), shows the edge dislocations and Cu atoms are interpenetrated in to the twin boundaries, (g) Intensity profile along the twin boundary in Figure 6(f), where the disparity of the intensity in the Au-rich and Cu-rich atomic columns can be observed.

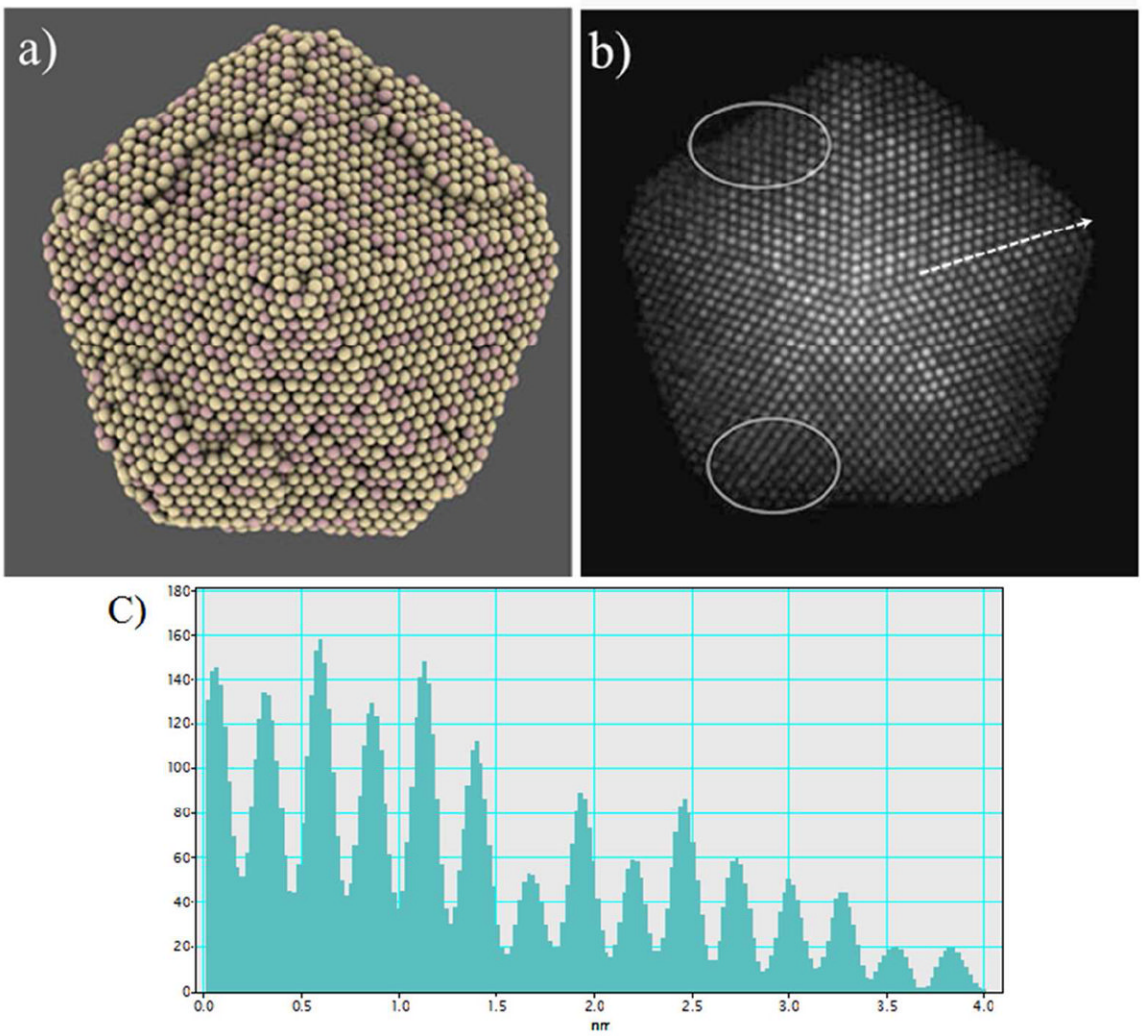

Figure 7.

(a) Simulated decahedral Au-Cu core-shell nanoparticle, where a partial atomic layer has been formed at the vicinity of the vertices of the particle. (b) STEM simulated micrograph of the particle in Figure (a) where white ovals represent partial layers. The regions with the partial atomic layers appear as lattice mismatches in the micrograph, just as in Figure 6. (c) Intensity profile along the twin boundary of STEM simulated image (along white arrow in Figure 7(b)), where the disparity of the intensity in the Au-rich and Cu-rich atomic columns can be observed.